Optics & Laser Technology 148 (2022) 107665

Contents lists available at ScienceDirect

Optics and Laser Technology

journal homepage: www.elsevier.com/locate/optlastec

Formation characteristics of nickel-based diamond abrasive segment by selective laser melting

Shuai Li [a,b], Bi Zhang [b,*], Qinghong Jiang [b], Huili Han [b], Jiale Wen [b], Cong Zhou [b]

[a] School of Mechatronics Engineering, Harbin Institute of Technology, Harbin 150001, China
[b] Department of Mechanical and Energy Engineering, Southern University of Science and Technology, Shenzhen 518055, China

ARTICLE INFO

Keywords:
Selective laser melting
Grinding wheel
Balling phenomenon
Spatter
Porosity

ABSTRACT

Selective Laser Melting (SLM) technique provides an alternative to fabricating a metal bond grinding wheel with a high porosity ratio and controllably complex geometries. In this paper, SLM is applied to making nickel-based diamond abrasive segments based on single-tracks SLM tests. The characteristics of the SLMed wheel segments are investigated through analyses on morphology, porosity, cracks, and diamond grains. Balling phenomenon of the Ni-Cr alloys, which leads to the rough surface and porosities, is observed through the surface and cross-sectional observations. The porosity ratio of the as-built abrasive segment ranges from 22.6% to 27.3%. Two types of diamond spatters, entrainment-driven and vapor-driven diamond spatters, are formed in the SLM process based on the observation by a high-speed video camera. Diamond spatters are considered the main cause of the balling phenomenon. Based on microstructure and hardness measurements, the eutectic structure and granular crystallites result in high hardness and increase the cracking susceptibility of the Ni-Cr alloys. This paper reveals the formation characteristics of the SLMed nickel-based wheel segments and the mechanism of porosity formation in the SLM process.

1. Introduction

Grinding is an essential process in precision manufacturing and has been applied to optics, aerospace, electronics, and automotive. A grinding wheel is a basic tool in controlling the dimensional accuracy and surface quality of a workpiece. It is basically composed of abrasives, bond material, and porosity, among which the bond material determines the key properties of a grinding wheel, such as strength, hardness, abrasive bonding strength, and self-sharpening ability. Compared with vitrified or resin bonds, metal bonds possess higher strength, stiffness, and thermal conductivity [1–3]. Furthermore, the addition of transition metals (Ti, Cr, Co) to a metal bond diamond grinding wheel can greatly enhance the bonding strength to diamond grains, due to chemical reactions at the interface [4,5]. The metal-bond wheels are widely applied to grinding difficult-to-machine materials, such as semiconductors, glasses, and ceramics [3,6].

Nevertheless, the high strength of a metal bond reduces the self-sharpening ability, leading to worn abrasives that can hardly fall off a grinding wheel. Surface and subsurface defects can be easily introduced in a machined workpiece by the worn abrasives. Pores in a grinding wheel can improve the self-sharpening ability, and provide sufficient space to accommodate debris and grinding coolant, suppressing temperature rise and workpiece burn [7]. The conventional metal-bond diamond grinding wheels fabricated by electroplating and brazing only have a thin abrasive layer with a limited porosity [5,8,9]. Hot pressing sintering (HPS) can fabricate porous grinding wheels by the addition of pore-forming agents, such as carbamide, polymethyl methacrylate, ice, and alumina bubbles [10,11]. Generally, uniformly distributed pores are desired for a grinding wheel. The pore size cannot be very large, because otherwise both flexural strength and bonding strength to diamond grains can be greatly reduced [12]. The porosity and pore structure should be determined with consideration of the mechanical properties of the grinding wheel. For the HPS technique, the porosity and pore structures mainly depend on the content and shape of pore-forming agents, but the pore distribution can be hardly controlled. Moreover, it is difficult to fabricate patterned grinding wheels with complex structures by conventional techniques.

Additive manufacturing (AM) technique is capable of producing complex parts through a layer-by-layer strategy and its application has been extended to aerospace, automotive, medicine, and many other industries [13,14]. AM provides an efficient and cost-effective solution to fabricate porous structure with micrometer-sized pores (2–30 μm)

* Corresponding author.
E-mail address: zhangb@sustech.edu.cn (B. Zhang).

https://doi.org/10.1016/j.optlastec.2021.107665
Received 19 May 2021; Received in revised form 29 October 2021; Accepted 8 November 2021
Available online 11 December 2021

and lattice structure with pores over ~100 μm [15]. Applying AM to fabricating porous metal-bond grinding wheels with particular geometries or profiles has been proved feasible by the previous studies [16,17,18]. For example, arrayed internal cooling holes could also be obtained by selective laser sintering to improve the performance of grinding wheels [19]. Besides, based on the layer-by-layer strategy, diamond grains could be arranged in each layer to build a 3D-patterned grinding wheel [20]. Aluminum-bond diamond grinding wheels with a porosity of 50% or higher were fabricated by Selective Laser Melting (SLM) in order to enhance cooling efficiency [16,21,22]. The pore morphology and porosity ratio could be controlled by the structure design so as to improve the grinding performance in varying degrees. By the laser powder bed fusion technique (LPBF), the NiTi bond diamond grinding tools were produced and showed promising abrasive capabilities [23]. Due to the existence of diamond grains, the surfaces of the fabricated parts were comparably rougher with some balling materials, and a crackling sound was made during the SLM process.

SLM possesses higher accuracy than most other laser additive techniques and shows a great potential in fabricating complex metal-based grinding wheels. However, there have been relatively few studies on the formation mechanism of a diamond wheel by SLM. This paper aims at applying SLM to fabricating a nickel-based grinding wheel and studying the formation characteristics of diamond abrasive segments. Firstly, single-track tests were carried out for the guidance of the diamond abrasive segment fabrication. Secondly, the formation characteristics of the SLMed abrasive segments were investigated in terms of surface and cross-sectional observations. The microstructure of the bond-abrasive layers was investigated to reveal the crack formation mechanisms of the bond material. Moreover, diamond spatters were observed with a high-speed video camera in the laser scanning process. The balling phenomenon and porosity formation are analyzed with the consideration of the influence of diamond spattering during the SLM process.

2. Experimental details

2.1. Materials and instruments

Commercial gas-atomized Ni-Cr pre-alloyed powders were used as the bond material with a particle range of 41 μm (D_{10}) - 89 μm (D_{90}), as shown in Fig. 1(a). The chemical compositions of Ni-Cr alloy were 7.0% Cr, 3.1% B, 4.5% Si, 3.0% Fe, and 82.4% Ni in weight percent. Ni-Cr alloys are usually used for brazing diamond tools because of the high hardness and toughness. The existence of Cr enhances the wettability and bond strength of diamond grains due to the formation of metal carbides. B and Si are favorable in lowering the melting point of the bond material, which is about 970–1,000 °C in this paper. Synthetic diamond grains ranging from 106 μm to 125 μm were employed and mixed with the Ni-Cr alloy powders by a 3D mixer for 3 h. The volume concentration of the diamond grains was set at 15% and the morphology of the mixed powders is shown in Fig. 1(b). AISI 1045 steel was used as the substrate material.

Ni-Cr/diamond segments were formed in an SLM equipment (Dimetal-100, Guangzhou Laseradd Technology Co., Ltd., China) with a maximum laser power of 500 W. The forming process of the abrasive segment by SLM is illustrated in Fig. 1(c), during which Ni-Cr alloy powders were melted in an orthogonal scanning strategy and served as bond material. In this paper, the laser with a 2 mm positive focus shift was applied to increasing the Gaussian beam diameter which was measured as around 120 μm by a laser beam diagnostics device. All the experiments were conducted in an Argon atmosphere with an oxygen content < 0.1%.

2.2. Single track formation

To obtain guidance to the parameter selection for the fabrication of abrasive segments, a series of single-track SLM tests were first conducted on the basis of analysis on the melt pool width (w) and depth (d) variation with the processing parameters. The mixed powder layer was 80 μm thick. Four sets of single track SLM tests were performed at a scanning speed ranging in $V = 200$–500 mm/s at a step size of 100 mm/s, and laser power $P = 60$ W–160 W at a step size of 20 W, as listed in Table 1. Both the melt pool width and depth were measured on three different cross-sections perpendicular to the scanning direction and the results are shown in Fig. 2. Due to the instability of the interaction between the laser beam with the Ni-Cr powders and diamond grains, the melt pool width and depth varied along the scanned tracks. A linear relationship between the melt pool width and Linear Energy Density (LED, L), which is defined as the ratio of laser power P to scanning speed V, is obtained in Fig. 2(a) and shown in a fitting formula as,

$$w = 260.27L + 108.30 \tag{1}$$

The linear fit of the melt pool width can be used to determine the hatch space.

Based on the previous studies on the keyhole transition, the melt pool depth is a function of the ratio of deposition energy density ΔH to the enthalpy at melting h_s [24],

$$d \propto \frac{\Delta H}{h_s} = \frac{AP}{\pi h_s \sqrt{DV\sigma^3}} \tag{2}$$

where A is laser absorptivity and D is the thermal diffusivity of the molten Ni-Cr alloy powders. Thermal diffusivity D and enthalpy at melting h_s are constants for the specific material. Melt pool depth d is

Table 1
SLM processing parameters for single tracks.

Processing parameters	Values
Laser spot size, σ (μm)	120
Powder layer thickness, h (μm)	80
Laser power, P (W)	60, 80, 100, 120, 140, 160
Scanning velocity, V (mm/s)	200, 300, 400, 500

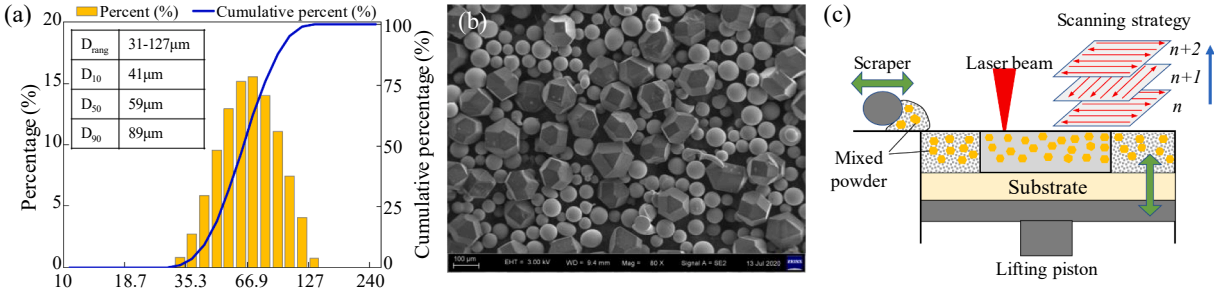

Fig. 1. (a) Particle range of Ni-Cr alloy powers, (b) SEM image of the mixed powders (diamond 106–125 μm) and (c) schematic diagram of abrasive segment fabrication by SLM.

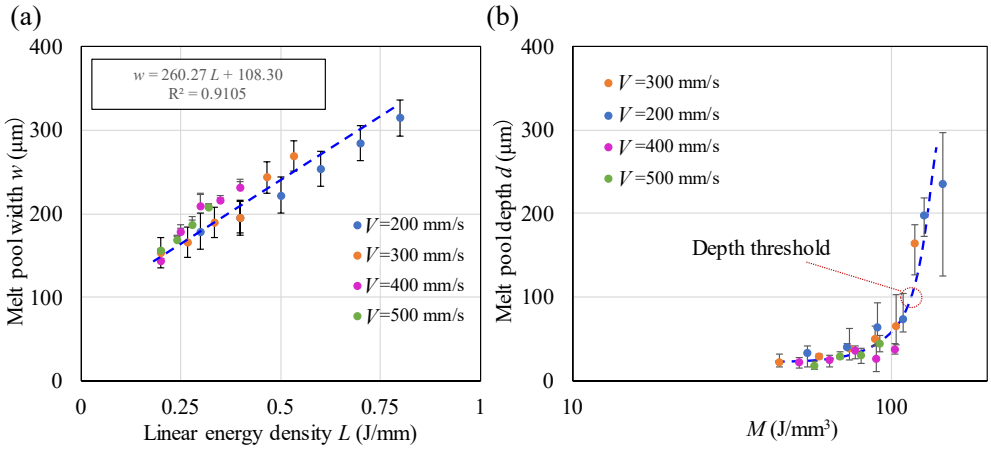

Fig. 2. Variations of (a) the melt pool width with LED and (b) depth with M on a semi-log scale.

mainly influenced by laser power P, scanning velocity V, and laser absorptivity A. The parameters P and V can be incorporated in one term M, as a controllable factor,

$$M = \frac{P}{\sqrt{DV\sigma^3}} \tag{3}$$

where thermal diffusivity D is calculated as 3.51×10^{-6} m^2/s [25] and laser spot size σ was around 120 μm. Fig. 2(b) shows the distribution of melt pool depth in terms of M on a semi-log scale, which can help choose processing parameters for an appropriate melt pool depth. The melt pool depth grows exponentially with the controllable factor M which is proportional to the ratio $P/\sqrt{V}$. The exponentially increasing slope mainly results from the increased laser absorptivity when a depression cavity occurs in the melt pool. In particular, the occurrence of the keyhole cavity in the melt pool greatly enhances the laser absorption due to the induced plasma [26], causing a rapid increase in the melt pool depth with M. It is appropriate to limit the melt pool depth to the powder layer thickness for lowering the residual thermal stress. A large melt pool depth brings excessive remelting of the previous layers and induces a large thermal deformation, leading to high residual thermal stress after the melting process [14]. The depth threshold is approximately at $M =$ 115 J/mm^3 in this paper, as exhibited in Fig. 2(b).

2.3. Experimental procedure

Based on the results in Fig. 2, nine abrasive segments were built at three different laser power levels (P = 80, 100, 120 W) and three scanning speeds (V = 200, 300, 400 mm/s). The hatch space was 0.7 times the melt pool width calculated by Eq. (1). To increase the bonding strength with the substrate, four layers of the Ni-Cr alloy were built on the substrate prior to the fabrication of abrasive segments. The surface morphology and roughness of the SLMed abrasive segments were measured by the confocal laser scanning microscopy (Keyence, VK-X1000). The porosity ratios were tested by the Archimedes method. A high-speed video camera (X113, Qianyanlang) was implemented to observe the motion of diamond grains during the laser scanning process at 3 kfps. For the illumination of the observing region, a diode laser light source was applied with the high-speed camera. The microstructure of the bond material was investigated by the scanning electron microscopy (SEM, Zeiss Merlin) and the X-ray diffractometry (XRD, Rigaku Smartlab).

3. Results

3.1. Surface morphology

Different from a dense Ni-Cr alloy structure, a porous structure is favorable to a diamond wheel segment. In this paper, porous abrasive segments were fabricated by SLM under different parametric conditions, as demonstrated in Fig. 3(a). Balling phenomenon was observed in the fabrication process of abrasive segments, which induced a large amount of balling materials on the top surface and was evidenced by the different levels of brightness and smoothness of the segments. The corresponding surface morphologies were measured and exhibited in Fig. 3 (b), showing a variation of the balling size in general. The balling materials above the average surface are in red, while the cavities below the average surface are blue in Fig. 3(b). The surface morphologies indicate that an increase in laser power or a decrease in scanning velocity could contribute to a smoother surface with a smaller balling size and fewer cavities, which mainly results from an increased LED value. The decrease in balling size with an increased LED can be verified by the SEM images of the top surface at a high magnification in Fig. 3(c). At P = 80 W and V = 400 mm/s (LED = 0.2 J/mm), large balling materials and deep cavities were formed due to insufficient laser energy. When LED was increased to 0.6 J/mm, the balling size was decreased to around 300 μm. In Fig. 3(c), it was found that diamond grains adhered to Ni-Cr alloy balls.

The surface roughnesses Sa and Sz, representing the arithmetic mean and maximum height of the surface profile, respectively, were shown in Fig. 4(a). The Sa decreased linearly with the increasing LED from 102 μm to 80 μm. The decrease in both Sa and Sz with the increasing LED resulted from a weakened melt balling effect. The bearing ratio, a ratio of the cross-sectional area at any specified depth to the evaluation area, of the three segments (3, 5, and 7) was measured along the depth from the top surface, as shown in Fig. 4(b). The bearing ratio of abrasive segment 7 with the maximum LED of 0.6 J/mm was larger than those at any depth due to the comparably small and dense balling materials. At a depth less than 400 μm, the bearing ratio of abrasive segment 3 (LED = 0.2 J/mm) was larger than that of segment 5 (LED = 0.33 J/mm) because a smaller LED induced larger balling sizes, and vice versa. However, abrasive segment 3 showed a bearing ratio smaller than that of segment 5 at a depth larger than 400 μm, due to the existence of deep cavities, as shown in Fig. 3(b).

3.2. Porosity

An insight study was conducted to characterize the balling phenomenon through the cross-sectional observations, as shown in Fig. 5. An as-built segment was cut along the building direction and processed

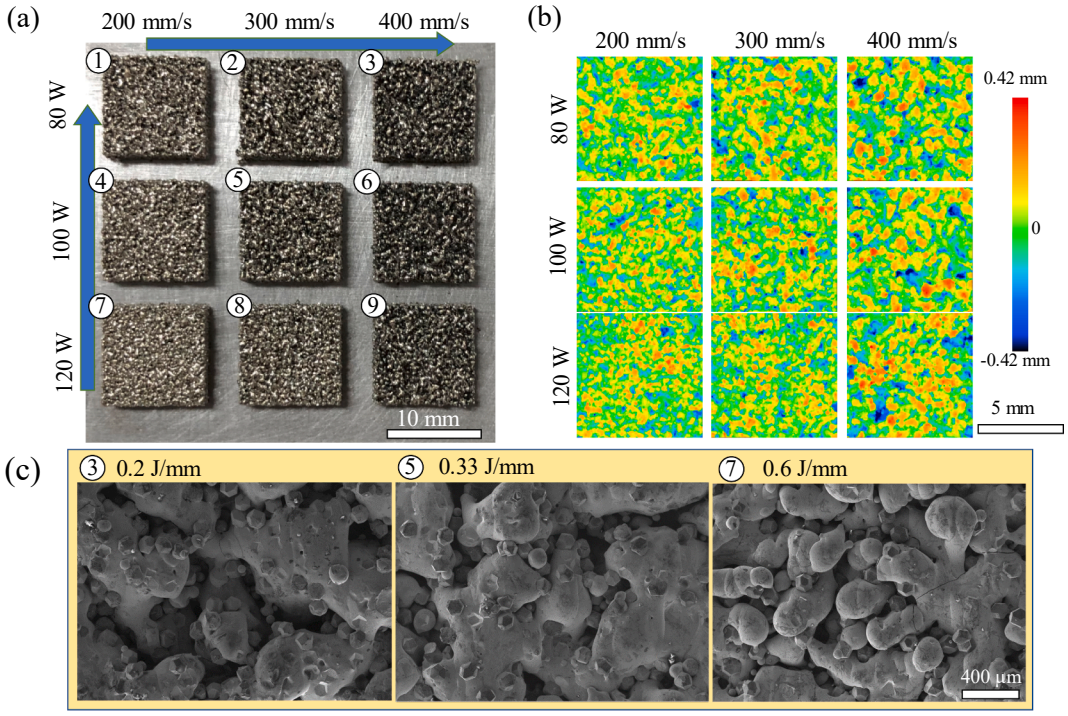

Fig. 3. Surface characteristics of the SLMed segments: (a) surface observations; (b) surface morphologies; (c) variation of balling size with LED.

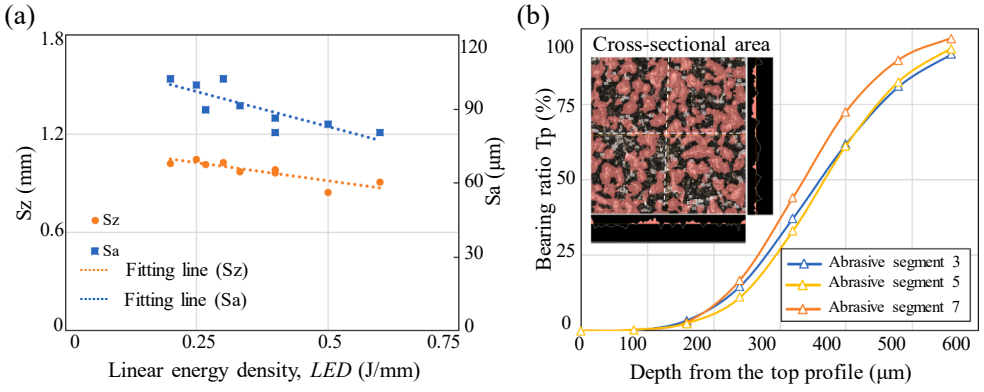

Fig. 4. Measurement results of (a) surface roughness and (b) bearing ratio of the as-built segments.

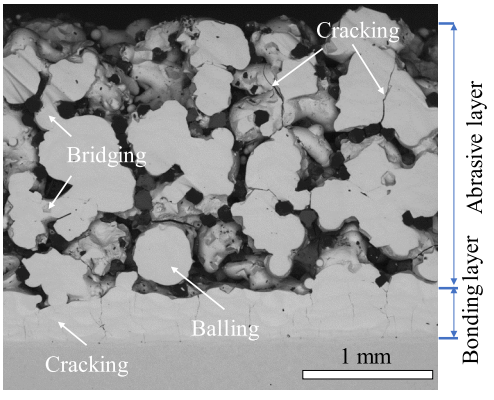

Fig. 5. Cross-sectional analysis on the as-built abrasive segment.

by sanding and polishing successively. As demonstrated in Fig. 5, after 30 layers of deposition, the bond material presented either spherical or irregular shapes on an abrasive segment. The bridging phenomenon was identified between the adjacent balling materials and thus porosities were produced inside the abrasive segment. The strength of the as-built segment with a larger balling size would be weakened due to a decrease in the bridging materials. In Fig. 5, the diamond grains are mainly distributed on the periphery of the bond materials. Diamond grains were the main cause of the balling and bridging phenomena which were hardly observed in the SLMed Ni-Cr alloy samples. On the one hand, the addition of diamond grains weakens the melt fluidity and blocks the molten materials to flow during the laser melting process [27,28]. On the other hand, diamond spatters are easily triggered in SLM to cause an inhomogeneous mixed powder layer [23,29], which will be further investigated in the following section.

The balling and bridging phenomena help create porosities in the abrasive segment, which is necessary for a grinding wheel. The porosity ratio of each SLMed abrasive segment was tested three times and the variation with LED is shown in Fig. 6. The porosity ratio varied in a

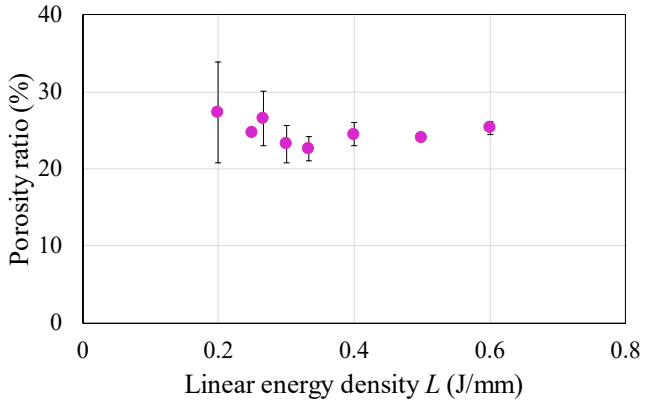

Fig. 6. Porosity ratio variation of the SLMed abrasive segments with LED.

range from 22.6% to 27.3%. With the increase of LED, the porosity first decreased from 27.3% to 22.6% and then slightly increased to 25.3%. The increased LED could reduce the balling size and result in a decreased porosity. However, a further increase in LED would trigger serious diamond spatter and thus more porosity formation. For a fixed ratio of diamond grains to the bond materials, the amount of diamond spatter might be limited due to the fixed ratio, leading to a limited increase in the porosity ratio.

3.3. Diamond spattering

Diamond spattering is triggered by the high-speed metal vapor induced by the evaporation of Ni-Cr alloy, which was evidenced by a crackling sound during the SLM process that was not heard during the fabrication of Ni-Cr alloy samples. A high-speed video camera was implemented to observe the diamond spattering for investigation on the mechanism of porosity formation, as shown in Fig. 7. To enhance observability, a light filter was used although differentiating diamond grains from Ni-Cr alloy powders was still a challenge because the light filter caused color losses. In Fig. 7(a), the motion of diamond grains during the laser scanning process was recorded. As the scanning laser beam passed by a diamond grain, the grain is blown toward the melt pool, and accelerated upward and forward along the scanning direction, as shown by the red dotted line in Fig. 7(a). During the powder melting process, a metal vapor is generated to induce an inward gas flow toward the laser spot, resulting in a flow field behind the melt pool. The diamond grain was driven by a gas flow field and moved toward the melt pool. A similar motion of the metal powders on both sides of the scanned track was also observed, as depicted by the blue arrows, which is called the entrainment phenomenon [30]. Under the strike of the metal vapor, the entrained diamond grains and metal powders were accelerated and ejected by the metal vapor, resulting in entrainment-driven spatters. The velocity of the entrained diamond grains was comparably lower than that by the ejection of metal vapor directly.

As the laser beam strikes directly on a diamond grain, part of the laser beam is reflected by the diamond surface, resulting in a shining region because of beam scattering, as shown in Fig. 7(b)-(ii). Under both the transmitted and reflected laser beam interactions, the Ni-Cr alloy powders around the diamond grain would partially be melted and adhere to the diamond surfaces. The diamond grains with the adhered powders would be ejected directly upward by the metal vapor, leading to a vapor-driven diamond spatter. In this paper, both entrainment-driven and vapor-driven diamond spatters were responsible for the crackling sound in the SLM process. Due to the residual heat of the melt pool and the induced gas flow, partially melted Ni-Cr alloy powders collided and adhered with each other, causing powder agglomeration, as shown in Fig. 7(b)-(iii). Spattering and agglomeration behaviors are clearly shown in the supplementary materials (Video 1 and Video 2).

3.4. Crack formation and microstructure

Cracks were found in both bonding and abrasive layers, as shown in Fig. 5. Due to the high cooling rate in the SLM process, a high level of thermal stress can be introduced in the deposited materials and leads to severe solidification cracking/hot cracking [31]. The microstructure

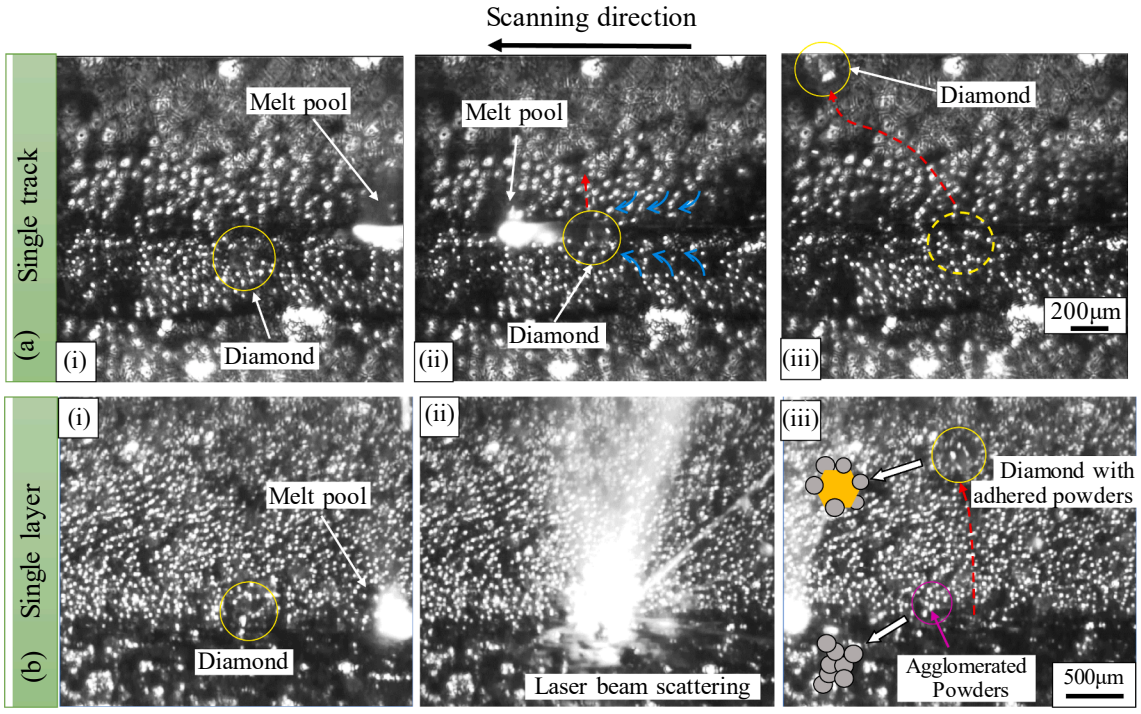

Fig. 7. The spattering behavior of diamond grains (a) beside the scanning track; (b) on the scanning track resulting in adhered powders to the diamond and agglomerated powders.

was analyzed to evaluate the crack sensitivity of the Ni-Cr bond material. The cross-section parallel to the building direction of an SLMed Ni-Cr alloy sample was sanded, polished, and finally etched by a mixed solution of HF, HNO_3, and H_2O (7 ml, 3 ml, and 5 ml) for 10 sec. The microstructures of two overlapping melt pools are shown in Fig. 8(a). A clear interface divided a melt pool into two regions: a dendrites region and a granular crystallites region. Because the eutectic structures are commonly formed with the Ni-Cr self-fluxing alloy, the structure observed in the zoomed-in view of Region 1 was inferred as the Ni-Si eutectics according to the previous research [32]. Besides, a number of small granular crystallites were present around the melt pool boundary. The size of the eutectic structure and granular crystallites decreased along the inverse heat flux direction. In the heat affected zone (HAZ) [33], granular crystallites with smaller sizes were formed. The size of the orientated dendrites in Region 2 was around 1 μm. According to an XRD analysis, γ-Ni, Ni_3Si, Ni_3B, and CrB phases were detected in the SLMed sample. The granular crystallites in Fig. 8(a) were inferred as precipitates of boride and chromium compounds. The precipitates, eutectic structure, and fine dendrites contributed to a high hardness of the material, reaching around 7.2 GPa. Wear resistance of the bond material will be greatly enhanced, and brittleness is also increased, resulting in a high-level crack sensitivity particularly for the SLMed sample.

3.5. Diamond grains

In a grinding wheel, the intact and well-bonded diamond grains are favorable to improving the grinding efficiency and wheel life. The morphology of diamond grains in the SLMed abrasive segments was analyzed. In Fig. 9(a), the Ni-Cr alloy climbed up along the diamond surface due to the existence of Cr, indicating a good wettability and bonding strength between the two. However, due to the combined thermal effect of laser irradiation and the catalytic effect of the transition metals of Ni and Cr, graphitization of the diamond grains was found at a high LED value (0.6 J/mm), as presented in Fig. 9(b). Since the laser energy follows the Gaussian distribution, it is easy to reach the graphitization temperature (approximately 1500 °C in the vacuum or an inert gas environment) at the laser spot center even if in a short heating process [18]. Graphitization would greatly deteriorate the strength of a diamond grain and should be avoided by controlling the processing parameters or laser energy distribution.

4. Discussion

Different from the fabrication of alloy parts in SLM, diamond spattering is speculated as the major cause of balling phenomenon, rough surface, and porosities in the fabrication of a nickel-based grinding wheel. At a low LED value, large and deep cavities tend to be generated because of the larger balling size, leading to higher surface roughness and porosity ratio. As the LED value was increased, smaller balls were formed and connected with each other. Uniformly distributed small pores were generated within an abrasive segment, resulting in a comparably denser segment. However, with a further increase in LED value, more diamond grains were lost due to serious diamond spattering. Thus, the porosity ratio of the abrasive segment increases slightly with much a higher LED value, as shown in Fig. 6.

Spattering is a common physical phenomenon in the SLM process that is mainly associated with the metal vapor and recoil pressure [27,30]. When the laser beam strikes the Ni-Cr alloy powders, a melt pool is formed and intense evaporation occurs at the top surface, producing a high-speed metal vapor, as depicted in Fig. 10(a). Recoil pressure is subsequently induced and creates a depression in the melt pool. The velocity of the metal vapor can reach a speed higher than 150 m/s [34]. Under the effect of high-speed metal vapor, diamond grains are ejected directly, resulting in vapor-driven diamond spattering. In the SLM process for metallic alloys, droplet spatters are produced by the effect of metal vapor and Marangoni force as the molten materials acquire enough kinetic energy to overcome the surface tension. According to the study of Sonny Ly [30], droplet spattering shares a small proportion of the total spatters whereas the entrainment-driven spattering takes a larger proportion. Accompanying with the metal vapor, an inward gas flow field is induced to drive the nearby powders towards the melt pool, forming the so-called entrainment phenomenon [27,35], as illustrated in Fig. 7(a). The entrained powders move toward the melt pool and are blown away under the impact of the high-speed metal vapor, resulting in hot spatters irradiated by the laser beam and cold spatters. Some entrained powders close enough will be blended into the melt pool, as depicted in Fig. 10(a). Due to the entrainment phenomenon, a denudation zone with fewer powders is formed, as the dark grey region shown in Fig. 10(b).

Based on the observations in Fig. 7 and the above analysis, both the entrainment-driven and vapor-driven diamond spattering are generated in the fabrication of abrasive segments in SLM. Moreover, diamond spattering is more easily triggered than metallic powder spattering because of the weak bonding force between the solid diamond grains and the liquid melt pool. The bonding force mainly results from the

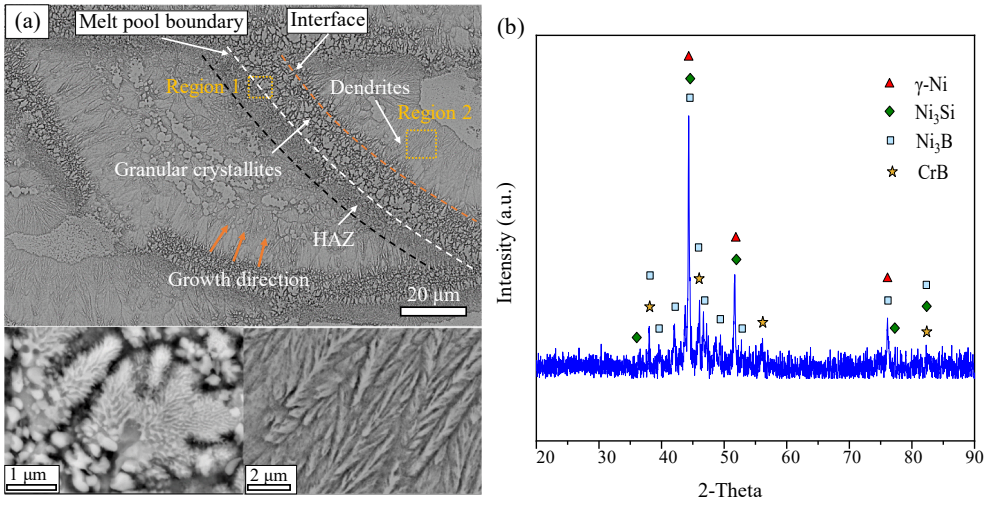

Fig. 8. (a) SEM observation of the microstructure and (b) XRD patterns of the SLMed Ni-Cr alloy part.

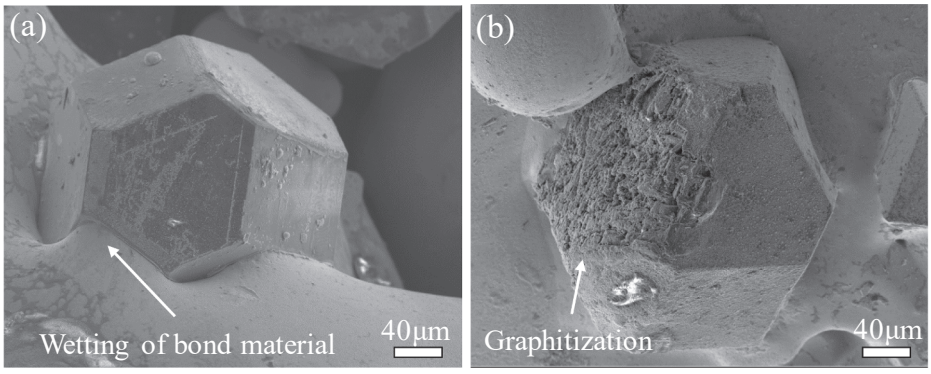

Fig. 9. Morphologies of diamond grains (a) wetting of the bond material and (b) surface graphitization of a diamond grain.

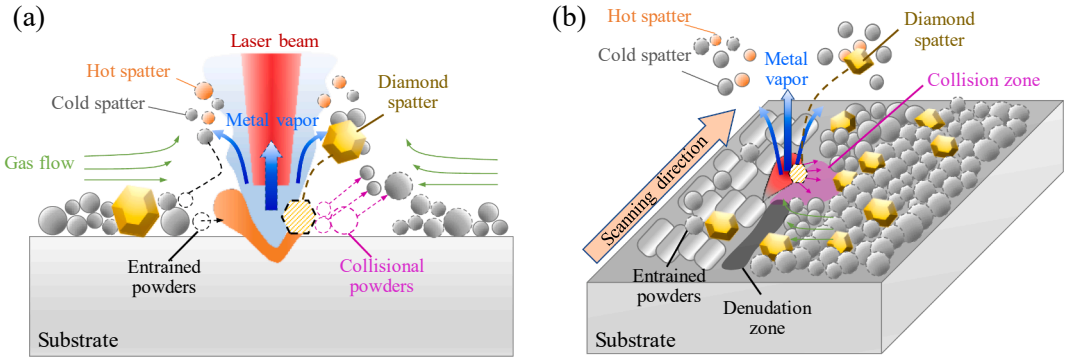

Fig. 10. Schematic illustration of the diamond spattering (a) in two dimensions and (b) three dimensions as the laser beam scans by a diamond grain.

surface tension, which is much smaller than the ejection force from the metal vapor. Therefore, diamond grains will be ejected away even though when they are in contact with the melt pool. Especially for large size diamond grains, a smaller contact area with a liquid melt pool results in weaker bonding which can be easily broken off under the effect of metal vapor and the inward gas flow field.

As diamond grains are ejected outward, the surrounding powders are influenced, which results in a crowd of collisional powders, as illustrated in Fig. 10(a). The collisional powders caused by the diamond spattering were observed in the high-speed video, as shown in Fig. 11. As a diamond grain is passed by the laser beam, the grain gains enough kinetic energy from the metal vapor to spatter away. The outward moving diamond grain collides with the surrounding powders, further producing a number of collisional powders which erupt outward and lead to a collision zone. Few powders exist in the collision zone and the width of the collision zone is almost three times the laser beam diameter. The formation of the collision zone is clearly shown in Supplementary Video 3. Accordingly, it is inferred that a bigger diamond grain causes a larger collision zone.

In this paper, diamond spattering is inferred as the key factor for the balling phenomenon and porosity formation of the SLMed abrasive segments. On the one hand, with diamond grains larger than the layer thickness in the powder layer, the spattering diamond grains induce serious material losses and cause incomplete melt pools, as shown in Fig. 10(a). At the same time, diamond grains can block the liquid melt pool from flowing, resulting in a reduced viscosity which was also reported in the previous studies on the diamond-based composites [29]. Consequently, discontinuous melting tracks are prone to form after laser scanning. On the other hand, diamond spattering causes collision zones and alters the layer thickness. Furthermore, bumps are produced in the powder layer due to the diamond spatters and the aggregated powders. The formation of a bump caused by diamond spatters and aggregated powders was recorded and clearly shown in Supplementary Video 4, demonstrating a non-uniform layer thickness. Thus, discontinuous melting tracks are produced with a non-uniform powder layer.

With discontinuous melting tracks overlapping one by one, a number of pits are generated after laser scanning of the first mixed powder layer. The non-uniformity in layer thickness is aggravated in the successive powder layer because of the diamond spatters and agglomerated powders, as illustrated in Fig. 12(a). An increase in powder layer thickness

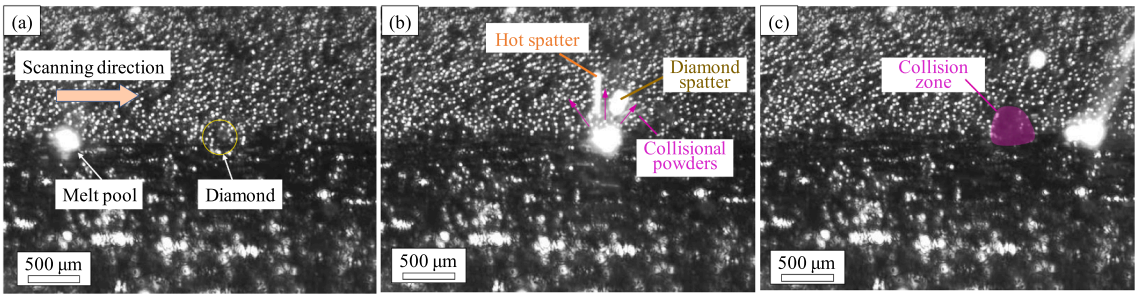

Fig. 11. Collisional powders and collision zone caused by diamond spattering.

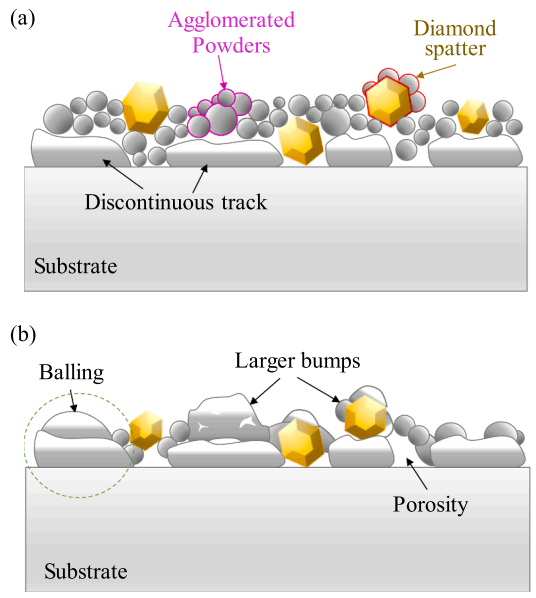

Fig. 12. Schematic illustration of the balling phenomenon and porosity formation (a) mixed powders laying on discontinuous tracks, (b) evolution of balling and porosity formations.

causes severer spattering, leading to large pores and cavities after deposition of the following layer [36]. Therefore, more material losses are induced by severer spattering at the location with thicker powders in the successive laser scanning process. In other words, the bond materials are mainly fused on the previously deposited materials, thus pits become larger, as shown in Fig. 12(b). Also, diamond spatters and aggregated powders can be fused onto the unevenly deposited layers, leading to larger bumps. With the deposition of the material layer-by-layer, discontinuous tracks evolve into spherical shapes due to the surface tension, i.e., balling phenomenon, resulting in interconnected porosities. With an increase of the LED value, the influence of discontinuous tracks and bumps on the following material deposition is weakened due to the increased penetration depth of the laser beam. Because the density of diamond grains is much smaller than the Ni-Cr alloy powders, the diamond grains are more prone to flow to the surface of the melted alloy.

5. Conclusions

In this paper, nickel-based abrasive segments were fabricated in SLM for grinding wheel applications. The formation characteristics were analyzed in terms of morphology evolution, porosity formation, and crack generation of the abrasive segments. The conclusions are summarized as follows:

1) Morphology of the SLMed abrasive segment is a result of balling and bridging phenomena. Balling of the bond materials is responsible for the rough surface, while an increase in LED can enhance the surface roughness and the bearing ratio of the SLMed abrasive segments.
2) Due to balling and bridging, porosities ranging from 22.6% to 27.3% were inducted into the abrasive segments. A larger balling size led to a higher porosity ratio. Both entrainment-driven and vapor-driven diamond spatters, which were triggered by the flow field behind the melt pool and the metal vapor respectively in the SLM process, were responsible for the generation of the balling phenomenon and the porosity.
3) The precipitates, eutectic, and fine dendrites structures can enhance the hardness of the bond material on one hand, but increase the crack sensitivity on the other hand.
4) A good wettability was formed between the bond material and diamond grains. Graphitization of the diamond grains occurred at a high LED value.
5) Further studies on the decrease in the crack sensitivity of the nickel bond material will be carried out to balance the strength and the self-sharpening ability of the SLMed wheel segments. In addition, the mechanical properties of the SLMed wheel segments and the practical grinding performance will be evaluated.

CRediT authorship contribution statement

Shuai Li: Conceptualization, Methodology, Investigation, Writing – original draft, Writing – review & editing. **Bi Zhang:** Conceptualization, Supervision, Funding acquisition, Writing – review & editing. **Qinghong Jiang:** Investigation, Software. **Huili Han:** Investigation, Data curation. **Jiale Wen:** Investigation. **Cong Zhou:** Writing – review & editing.

Declaration of Competing Interest

The authors declare that they have no known competing financial interests or personal relationships that could have appeared to influence the work reported in this paper.

Acknowledgments

The authors thank the Shenzhen Science and Technology Innovation Commission for the financial support numbered as KQTD20190929172505711, GJHZ20180411143506667, and JCYJ20170817111811303. This work was also supported by the Pico Center at SUSTech with support from the Presidential fund and Development and Reform Commission of Shenzhen Municipality.

Appendix A. Supplementary material

Supplementary data to this article can be found online at https://doi.org/10.1016/j.optlastec.2021.107665.

References

[1] J. Webster, M. Tricard, Innovations in abrasive products for precision grinding, CIRP Ann. - Manuf. Technol. 53 (2) (2004) 597–617, https://doi.org/10.1016/S0007-8506(07)60031-6.
[2] B. Denkena, T. Grove, V. Suntharakumaran, New profiling approach with geometrically defined cutting edges for sintered metal bonded CBN grinding layers, J. Mater. Process. Technol. 278 (2020) 116473, https://doi.org/10.1016/j.jmatprotec.2019.116473.
[3] B. Denkena, T. Grove, I. Bremer, L. Behrens, Design of bronze-bonded grinding wheel properties, CIRP Ann. - Manuf. Technol. 65 (1) (2016) 333–336, https://doi.org/10.1016/j.cirp.2016.04.096.
[4] P. Mukhopadhyay, A. Ghosh, On bond wear, grit-alloy interfacial chemistry and joint strength of synthetic diamond brazed with Ni-Cr-B-Si-Fe and Ti activated Ag-Cu filler alloys, Int. J. Refract. Met. Hard Mater. 72 (2018) 236–243, https://doi.org/10.1016/j.ijrmhm.2017.12.033.
[5] D.-Z. Duan, B. Xiao, W. Wang, Z.-Y. Zhang, B.o. Wang, P. Han, X.-Y. Ding, Interface characteristics and performance of pre-brazed diamond grains with Ni-Cr composite alloy, J. Alloys Compd. 644 (2015) 626–631, https://doi.org/10.1016/j.jallcom.2015.03.269.
[6] H. Deng, G. Chen, J. He, C. Zhou, H. Du, Y. Wang, Online, efficient and precision laser profiling of bronze-bonded diamond grinding wheels based on a single-layer deep-cutting intermittent feeding method, Opt. Laser Technol. 80 (2016) 41–50, https://doi.org/10.1016/j.optlastec.2015.12.021.
[7] X. Zhang, J. Jiang, S. Li, D. Wen, Laser textured Ti-6Al-4V surfaces and grinding performance evaluation using CBN grinding wheels, Opt. Laser Technol. 109 (2019) 389–400, https://doi.org/10.1016/j.optlastec.2018.08.027.
[8] J. Chen, D. Mu, X. Liao, G. Huang, H. Huang, X. Xu, H. Huang, Interfacial microstructure and mechanical properties of synthetic diamond brazed by Ni-Cr-P filler alloy, Int. J. Refract. Met. Hard Mater. 74 (2018) 52–60, https://doi.org/10.1016/j.ijrmhm.2018.03.005.
[9] H.-Z. Xiao, B. Xiao, H.-H. Wu, Interfacial characteristics and mechanical properties of the vacuum brazing diamond grains segment with Ni-Cr composite active filler and tungsten carbide reinforcement, J. Alloys Compd. 781 (2019) 226–234, https://doi.org/10.1016/j.jallcom.2018.12.106.

[10] B. Zhao, A.K. Gain, W. Ding, L. Zhang, X. Li, Y. Fu, A review on metallic porous materials: pore formation, mechanical properties, and their applications, Int. J. Adv. Manuf. Technol. 95 (5-8) (2018) 2641–2659, https://doi.org/10.1007/s00170-017-1415-6.
[11] C.-Y. Ma, W.-F. Ding, J.-H. Xu, Y.-C. Fu, Influence of alumina bubble particles on microstructure and mechanical strength in porous Cu-Sn-Ti metals, Mater. Des. 65 (2015) 50–56, https://doi.org/10.1016/j.matdes.2014.09.002.
[12] B. Zhao, W. Ding, Z. Chen, C. Yang, Pore structure design and grinding performance of porous metal-bonded CBN abrasive wheels fabricated by vacuum sintering, J. Manuf. Process. 44 (2019) 125–132, https://doi.org/10.1016/j.jmapro.2019.06.001.
[13] M. Anand, A.K. Das, Issues in fabrication of 3D components through DMLS Technique: A review, Opt. Laser Technol. 139 (2021) 106914, https://doi.org/10.1016/j.optlastec.2021.106914.
[14] Z. Yan, W. Liu, Z. Tang, X. Liu, N. Zhang, M. Li, H. Zhang, Review on thermal analysis in laser-based additive manufacturing, Opt. Laser Technol. 106 (2018) 427–441, https://doi.org/10.1016/j.optlastec.2018.04.034.
[15] G.H. Zeng, T. Song, Y.H. Dai, H.P. Tang, M. Yan, 3D printed breathable mould steel: Small micrometer-sized, interconnected pores by creatively introducing foaming agent to additive manufacturing, Mater. Des. 169 (2019) 107693, https://doi.org/10.1016/j.matdes.2019.107693.
[16] C. Tian, X. Li, H. Li, G. Guo, L. Wang, Y. Rong, The effect of porosity on the mechanical property of metal-bonded diamond grinding wheel fabricated by selective laser melting (SLM), Mater. Sci. Eng. A. 743 (2019) 697–706, https://doi.org/10.1016/j.msea.2018.11.138.
[17] K.D. Traxel, A. Bandyopadhyay, Diamond-reinforced cutting tools using laser-based additive manufacturing, Addit. Manuf. 37 (2021) 101602, https://doi.org/10.1016/j.addma.2020.101602.
[18] J. Gan, H. Gao, S. Wen, Y. Zhou, S. Tan, L. Duan, Simulation, forming process and mechanical property of Cu-Sn-Ti/diamond composites fabricated by selective laser melting, Int. J. Refract. Met. Hard Mater. 87 (2020) 105144, https://doi.org/10.1016/j.ijrmhm.2019.105144.
[19] Z.-J. Du, F.-L. Zhang, Q.-S. Xu, Y.-J. Huang, M.-C. Li, H.-P. Huang, C.-Y. Wang, Y.-M. Zhou, H.-Q. Tang, Selective laser sintering and grinding performance of resin bond diamond grinding wheels with arrayed internal cooling holes, Ceram. Int. 45 (16) (2019) 20873–20881, https://doi.org/10.1016/j.ceramint.2019.07.076.
[20] Y. Qiu, H. Huang, Research on the fabrication and grinding performance of 3-dimensional controllable abrasive arrangement wheels, Int. J. Adv. Manuf. Technol. 104 (5-8) (2019) 1839–1853, https://doi.org/10.1007/s00170-019-03900-1.
[21] C. Tian, X. Li, S. Zhang, G. Guo, L. Wang, Y. Rong, Study on design and performance of metal-bonded diamond grinding wheels fabricated by selective laser melting (SLM), Mater. Des. 156 (2018) 52–61, https://doi.org/10.1016/j.matdes.2018.06.029.
[22] C. Tian, X. Li, Z. Chen, G. Guo, L. Wang, Y. Rong, Study on formability, mechanical property and finite element modeling of 3D-printed composite for metal-bonded diamond grinding wheel application, J. Manuf. Process. 54 (2020) 38–47, https://doi.org/10.1016/j.jmapro.2020.02.028.
[23] B. Denkena, A. Krödel, J. Harmes, F. Kempf, T. Griemsmann, C. Hoff, J. Hermsdorf, S. Kaierle, Additive manufacturing of metal-bonded grinding tools, Int. J. Adv. Manuf. Technol. 107 (5-6) (2020) 2387–2395, https://doi.org/10.1007/s00170-020-05199-9.
[24] W.E. King, H.D. Barth, V.M. Castillo, G.F. Gallegos, J.W. Gibbs, D.E. Hahn, C. Kamath, A.M. Rubenchik, Observation of keyhole-mode laser melting in laser powder-bed fusion additive manufacturing, J. Mater. Process. Technol. 214 (12) (2014) 2915–2925, https://doi.org/10.1016/j.jmatprotec.2014.06.005.
[25] W. Jiang, J. Gong, S. Tu, H.u. Chen, Modelling of temperature field and residual stress of vacuum brazing for stainless steel plate-fin structure, J. Mater. Process. Technol. 209 (2) (2009) 1105–1110, https://doi.org/10.1016/j.jmatprotec.2008.03.031.
[26] Q. Gao, T. Yan, W. Ling, H. Bu, X. Zhan, H. Shen, Effect of vapor/plasma-liquid flow behavior on the keyhole oscillation in laser-MIG hybrid welding of Invar alloy, Opt. Laser Technol. 140 (2021) 107054, https://doi.org/10.1016/j.optlastec.2021.107054.
[27] D. Gu, Y.-C. Hagedorn, W. Meiners, K. Wissenbach, R. Poprawe, Nanocrystalline TiC reinforced Ti matrix bulk-form nanocomposites by Selective Laser Melting (SLM): Densification, growth mechanism and wear behavior, Compos. Sci. Technol. 71 (13) (2011) 1612–1620, https://doi.org/10.1016/j.compscitech.2011.07.010.
[28] Y. Ma, G. Ji, X.P. Li, C.Y. Chen, Z.Q. Tan, A. Addad, Z.Q. Li, T.B. Sercombe, J. P. Kruth, On the study of tailorable interface structure in a diamond/Al12Si composite processed by selective laser melting, Materialia. 5 (2019) 100242, https://doi.org/10.1016/j.mtla.2019.100242.
[29] L. Constantin, N. Kraiem, Z. Wu, B. Cui, J.-L. Battaglia, C. Garnier, J.-F. Silvain, Y. F. Lu, Manufacturing of complex diamond-based composite structures via laser powder-bed fusion, Addit. Manuf. 40 (2021) 101927, https://doi.org/10.1016/j.addma.2021.101927.
[30] S. Ly, A.M. Rubenchik, S.A. Khairallah, G. Guss, M.J. Matthews, Metal vapor micro-jet controls material redistribution in laser powder bed fusion additive manufacturing, Sci. Rep. 7 (1) (2017), https://doi.org/10.1038/s41598-017-04237-z.
[31] S.Y. Zhou, Y. Su, H. Wang, J. Enz, T. Ebel, M. Yan, Selective laser melting additive manufacturing of 7xxx series Al-Zn-Mg-Cu alloy: Cracking elimination by co-incorporation of Si and TiB2, Addit. Manuf. 36 (2020) 101458, https://doi.org/10.1016/j.addma.2020.101458.
[32] G. Yan, A. Bhowmik, B. Nagarajan, X.u. Song, S.C. Tan, M.J. Tan, Post-bond heat treatment effects on the wide gap transient liquid phase bonding of Inconel 718 with BNi-2 paste filler metal, Mater. Sci. Eng. A. 766 (2019) 138267, https://doi.org/10.1016/j.msea.2019.138267.
[33] Y. Li, K. Chen, N. Tamura, Mechanism of heat affected zone cracking in Ni-based superalloy DZ125L fabricated by laser 3D printing technique, Mater. Des. 150 (2018) 171–181, https://doi.org/10.1016/j.matdes.2018.04.032.
[34] P. Bidare, I. Bitharas, R.M. Ward, M.M. Attallah, A.J. Moore, Fluid and particle dynamics in laser powder bed fusion, Acta Mater. 142 (2018) 107–120, https://doi.org/10.1016/j.actamat.2017.09.051.
[35] M.J. Matthews, G. Guss, S.A. Khairallah, A.M. Rubenchik, P.J. Depond, W.E. King, Denudation of metal powder layers in laser powder bed fusion processes, Acta Mater. 114 (2016) 33–42, https://doi.org/10.1016/j.actamat.2016.05.017.
[36] Y. Zhang, G.S. Hong, D. Ye, K. Zhu, J.Y.H. Fuh, Extraction and evaluation of melt pool, plume and spatter information for powder-bed fusion AM process monitoring, Mater. Des. 156 (2018) 458–469, https://doi.org/10.1016/j.matdes.2018.07.002.